JOURNAL OF Materials CHEMISTRY

Bonding patterns and instabilities in the $m=2$ Ruddlesden–Popper phases: $LaSr_2Mn_2O_7$ and $La_2CaCu_2O_6$

Claudia Felser, Ram Seshadri, Astrid Leist and Wolfgang Tremel

Institut für Anorganische Chemie und Analytische Chemie, Johannes Gutenberg-Universität Becher Weg 24, Mainz D55099, Germany

We present the results of high level band structure calculations on the important layered compounds $LaSr_2Mn_2O_7$ and $La_2CaCu_2O_6$; both of which have the structure of the $m=2$ member of the Ruddlesden–Popper phases and comprise intergrowths of double perovskite slabs with rock-salt slabs. The cuprate additionally has an ordered oxygen defect. For further comparison, the band structure of tetragonal La_2CuO_4 has also been calculated. The manganite is a material exhibiting giant magnetoresistance (GMR) effects and the cuprates can be doped to give superconductors. The calculations have been performed using the TB-LMTO-ASA programs within the local (spin) density approximation L(S)DA; for the manganite, spin-polarized calculations result in a magnetic ground state; calculations on the ferromagnet and two antiferromagnetic structures are compared. The calculations show up similarities and differences between the bonding patterns of these two structurally related compounds that display widely different ground states when they are doped. The instabilities on or near the Fermi surface possibly implicated in the stabilization of the different ground states are, however, quite similar in character.

1 Introduction

The past few years have seen the technologically important phenomenon of giant or colossal negative magnetoresistance (GMR/CMR) becoming a part of the vocabulary of solid state and materials chemists, with the observation that certain oxides of manganese[1–4] and cobalt,[5,6] and also certain mixed transition metal sulfides[7] and oxides[8] show resistivities that decrease drastically on the application of (rather high) magnetic fields. As in the case of the high-T_c oxide superconductors, the search for this phenomenon in existing as well as novel materials has become an area of research being widely pursued. There is already clear evidence that many more systems might display GMR than is the case for high-T_c. The key physical features of the perovskite manganites that show GMR have been summarized by Goodenough and coworkers[9] who point out that the high-temperature paramagnetic phase is a polaronic conductor and the ferromagnetic (low-temperature) phase has extended states or remains polaronic depending on the metal–oxygen orbital overlap which in turn is governed by the perovskite tolerance factor t.[10] Some typical concerns regarding these systems remain, however, including the importance of Jahn–Teller distortions, the nature of the high-temperature insulating phase (where insulating loosely refers to the negative slope of the resistance–temperature curve) and the importance of correlation and disorder.

There is now a gathering belief that electronic instabilities near the Fermi surface as seen in accurate band structures and photoemission spectra of the cuprates are important for the superconductive pairing at low temperatures.[11,12] These instabilities manifest as van Hove singularities (vHS) and are seen as an X-shaped nesting of the Fermi surface in the ideal two-dimensional case. Magnetic fields are able to induce structural transitions in the manganites.[13] The rôle of magnetopolarons[14] in determining transport properties have been established. These and other factors suggest that unstable Fermi surfaces might be a characteristic feature of GMR materials as well.

It is of interest to understand bonding patterns in typical GMR manganites as obtained from high level band structure calculations. While one-electron calculations cannot be expected to yield details of many-body effects, in the ideal case the utility of such calculations might go beyond merely explaining the bonding situation found in a single composition to explain properties in related systems and even provide hints on what sort of materials might display similar phenomena.

In this paper, we report the results of spin-polarized, tight-binding electronic structure calculations performed using the linearised muffin-tin orbital (LMTO) method within the atomic sphere and local density approximations (ASA/LDA). The compounds studied were an approximation to a self-doped layered Ruddlesden–Popper manganite, $LaSr_2Mn_2O_7$, which is ferromagnetic, as well as two antiferromagnetic structures (one of them a supercell). The isostructural (but oxygen deficient) compound $La_2CaCu_2O_6$ which becomes superconducting on replacing some of the La with Sr has also been subject to calculations. For comparison, we have performed calculations on the structurally related layered oxide La_2CuO_4 in an approximate body-centered tetragonal cell. This last compound is the well known prototype of the layered copper oxide superconductors. As we will remark, there are striking similarities in the electronic structures of the compounds suggesting that similar instabilities on or near the Fermi surface are the signatures of the different broken-symmetry low-temperature ground states. The larger basal plane parameter and the presence of two different kinds of apical oxygen atoms in the metal–oxygen octahedra of the manganite result in some interesting differences in the band structures, which we highlight. The comparison also brings out the rôle of apical oxygen atoms, since in the three compounds, the natures of the apical oxygens are different.

1.1 The $(LnSr)_3Mn_2O_7$ system

These compound have the intergrowth $m=2$ Ruddlesden–Popper structure[15] and are thus closely related to the high-T_c superconductors.[16] A schematic of this structure and those of other Ruddlesden–Popper perovskites, $SrTiO_3$ ($m=\infty$) and tetragonal La_2CuO_4 ($m=1$) are displayed in Fig. 1 along with the oxygen defect $m=2$ structure of $La_2CaCu_2O_6$. The [010] projection is shown. The different shadings of atoms and polyhedra represent positions (0 and z/b) looking through the plane of the representation. Like the related perovskites, $(LnSr)MnO_3$,[17] the layered compounds $La_{1+x}Sr_{2-x}Mn_2O_7$ have been long known[18,19] as systems displaying Zener double exchange (DEX)[20] whereby electrons hop with spin memory. As a result of this, the paramagnetic–ferromagnetic transition

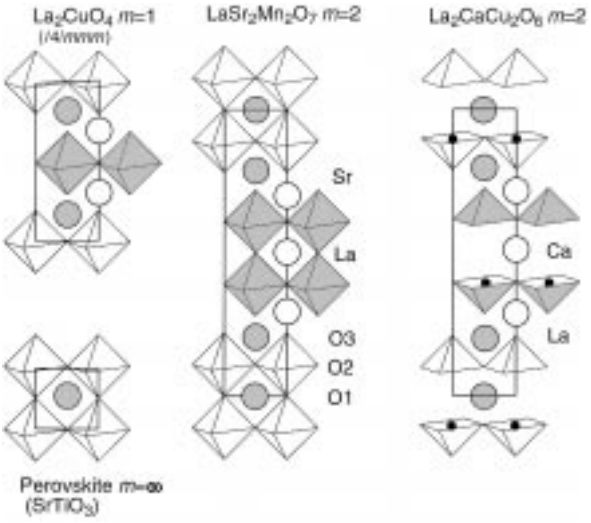

Fig. 1 Structures of typical $m=\infty$,1 and 2 Ruddlesden–Popper phases looking down the [010] direction. The polyhedra represent MO_x where M is the transition metal. The shading refers to the depth looking through the plane of the representation. Open implies $y/b=0$ and shaded implies $y/b=0.5$.

(near 130 K for $x=0.2$) is accompanied by the transition from a semiconductor to a poor metal. These systems have been re-examined in light of their displaying GMR in the metallic, low-temperature regime.[21,22] The salient features of this system are: ferromagnetism when $0.1 \leqslant x \leqslant 0.5$;[23] an absence of the ferromagnetic transition (and hence of a metallic phase) when La is replaced by smaller lanthanoids;[24–27] unusual structural changes (studied for $x=0.2$) as the metal–insulator transition is traversed[28,29] and as the lanthanoid is made smaller.[25] In the ferromagnetic compounds, the saturation value of the magnetic moment is usually of the order of 3 μ_B as opposed to the expected spin-only value of $(3.5+x/2)$ μ_B for ferromagnetic $La_{1+x}Sr_{2-x}Mn_2O_7$. Also of note is complex transport behaviour in the $x=0$ compound $LaSr_2Mn_2O_7$, which shows some evidence for the real-space ordering of holes as the temperature is lowered, accompanied by a transition to an antiferromagnetic state.[30] Difficulties in preparing pure samples give rise to novel microstructural features in these systems.[26,31,32]

We have chosen to perform high level calculations on an approximation to the structure of $LaSr_2Mn_2O_7$. While the crystal structure used in the calculation was taken from X-ray Rietveld refinements[30] and closely matched the neutron structure of $La_{1.2}Sr_{1.8}Mn_2O_7$,[28,29] La and Sr were taken to be fully ordered over the A lattice sites 2b and 4e. This allows the 'doping' to be achieved without taking recourse in superstructures. In the actual structure, most of the La is in the 4b site. While this artificial cation ordering might, in reality, be expected to affect physical properties considering the documented effect of disorder and strain on transport in the related perovskites,[33] within the LDA, these effects are negligible because La and Sr states are so far above the E_F. There can, however, be an effect of local potentials due to the different charges on these ions.[34]

As a model system, a desirable feature of $LaSr_2Mn_2O_7$, apart from the self-doping and the similarities with high-T_c compounds mentioned earlier, is that the *I*4/*mmm* crystal system allows direct visualizing of bonding patterns without the need for any coordinate transformations. The actual structure used was *I*4/*mmm*; $LaSr_2Mn_2O_7$, with the parameters $a=$ 3.8755 Å, $c=19.996$ Å. La and O1 occupy the special position 2b. Sr, Mn and O3 are in distinct 4e sites with $z=0.3180$ for Sr, $z=0.0977$ for Mn and $z=0.1976$ for O3. O2 is in the plane in the 8g site with $z=0.0950$. The two apical oxygens, O1 and O3, in this structure are distinct in that O1 links the two Mn in the double perovskite unit; O3, however, bonds with Mn only on one side. These oxygens are labelled in Fig. 1.

Two antiferromagnetic structures were used to perform further calculations. One was obtained by considering feromagnetic layers coupled antiferromagnetically along *c*. This is the so-called A-type antiferromagnetic structure. The other structure was obtained by constructing a hypothetical $\sqrt{2}a_P \times \sqrt{2}a_P \times c$ supercell of $LaSr_2Mn_2O_7$. In this supercell, the alternation of MnO_6 octahedra could allow charge ordering of the manganese provided the structure were relaxed during the calculation. The schematic structures of these antiferromagnets is displayed in Fig. 2(a) and (b), the latter being the supercell.

1.2 The $La_2CaCu_2O_6$ system

Superconductivity below 60 K is achieved by replacing La by Sr in this compound[35] and below 40 K through increasing the oxygen content.[36] The crystal structure used for the calculations was for *I*4/*mmm*: $La_{1.6}Sr_{0.4}CaCu_2O_6$.[37] However, we have neglected the Sr doping in our calculation, considering the La to fully occupy the 4e site with $z=0.17578$ and Ca to fully occupy the 2a site at (0,0,0). The O1 oxygen of the $LaSr_2Mn_2O_7$ structure is missing resulting in copper at the 4e site with $z=$ 0.58503 being surrounded by five oxygens in a square-pyramidal arrangement. However, any oxygen atoms intercalated into this structure would be expected to occupy the O1 site. Oxygen O2 in the plane is at 8g with $z=0.0823$ and the apical oxygen O3 at 4e with $z=0.2954$. The lattice parameters are $a=$ 3.8248 Å and $c=19.4286$ Å. A schematic structure is shown in Fig. 1. Note that this is a double layer cuprate without a complex charge reservoir, in contrast to the mercury, thallium, lead and bismuth cuprates. Compared with $YBa_2Cu_3O_{7-\delta}$, the band structure of this system is easier to understand since there are no CuO chains. The different crystallographic settings for the manganite and the cuprate are retained from the original publications.

1.3 The La_2CuO_4 system

The calculation on La_2CuO_4 presented for comparison considers a tetragonal *I*4/*mmm* unit cell instead of the observed orthorhombic *Bmab* unit cell. In the *I*4/*mmm*: La_2CuO_4 structure (Fig. 1) there is only one apical oxygen position and one position for La, both at 4e: O2 with $z=0.1732$ and La with $z=0.3640$. Cu and the in-plane oxygen O1 occupy the special positions 2a and 4c. The lattice parameters used were

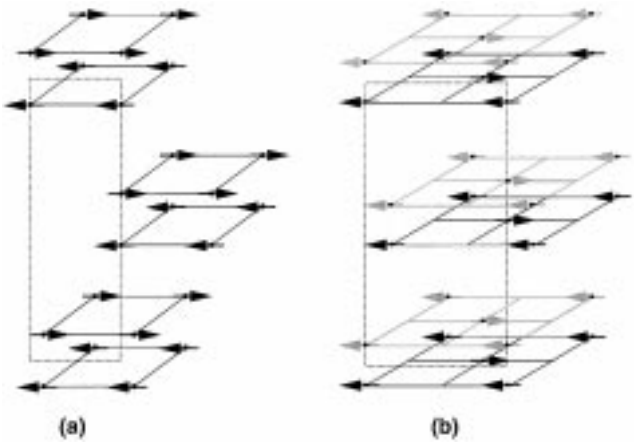

Fig. 2 Spin arrangements in the two antiferromagnetic $LaSr_2Mn_2O_7$ on which calculations have been performed: (a) is an A-type antiferromagnet and (b) is a $\sqrt{2}a_P \times \sqrt{2}a_P \times c$ superstructure

$a = 3.7265$ Å and $c = 12.870$ Å, obtained by transformation from the orthorhombic structure.

2 Reciprocal space and calculation procedure

Detailed band structure calculations on the *I*4/*mmm* structures of LaI_2,[38] of the $ThCr_2Si_2$ structure type[39] and, of course, certain high-T_c superconductors[40] exist, which make familiar the reciprocal space of the title compounds. The central Brillouin zone is as given in ref. 41, but we follow the standard labelling of refs. 38 and 40. It has the shape of a faceted box which is flat in the *z*-direction. The high symmetry points are Γ (0,0,0), X (π/a,π/a,0), Z ($2\pi/a$, 0,0) in the plane reciprocal to $z = 0$, and Z (0,0,π/c). Z repeats because of the body-centering in real space. The Brillouin zone is depicted in Fig. 3.

The LMTO method is rapidly becoming a convenient method of obtaining reliable band structures and bonding patterns for a variety of extended solids. The self-consistent calculations reported here were performed using the TB-LMTO-ASA codes from the Andersen group.[42] Detailed descriptions of the local density and local spin density approximations (LDA/LSDA) and the procedure by which reciprocal space integrations are performed and self-consistency is achieved, can be found elsewhere.[43] The basis sets consisted of 6s, 5d and 4f orbitals for La; 4s, 4p and 3d orbitals for Mn and Cu; 5s and 4d orbitals for Sr; 4s and 3d orbitals for Ca, and 2p orbitals for O. The 3s orbitals of O, 6p of La, 5p of Sr and 4p of Ca were treated by the downfolding technique. The atomic sphere approximation (ASA) relies on the partitioning of space into atom-centered spheres as well as empty spheres, the latter being crucial for structures that are not close-packed. The blowing up of the volumes of the atomic spheres and the selection of the radii and positions of the empty spheres are handled automatically[44] in the LMTO suite of programs with the caveat that atom-centered spheres do not have a volume overlap of more than 16%.

The number of irreducible *k* points used in the calculations were 349 for the manganites and for $La_2CaCu_2O_6$, and 498 for La_2CuO_4.

The band structures in the vicinity of the Fermi level allow important symmetry based conclusions to be drawn. More importantly, using the so-called 'fatband' representation, the exact orbital character of the individual bands can be understood. In this representation, each band is decorated with a width that is proportional to the sum of the weights of the corresponding orthonormal orbitals. In all the band structures shown, 'pure' orbital character corresponding to 100% character of a certain type of orbital is represented by decorating bands with a thickness of 2.5% of the total energy scale, in our case, 0.175 eV.

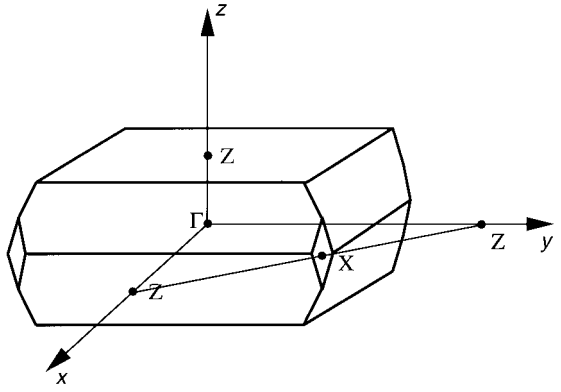

Fig. 3 Central Brillouin zone of the *I*4/*mmm* space group. Z in the primitive cell becomes Z in the plane in the neighboring cells because of the body-centering.

3 Densities of state

We commence with a discussion of the cuprates since, being non-magnetic, they are the simpler case.

3.1 Paramagnetic La_2CuO_4

The paramagnetic density of states of La_2CuO_4, seen in Fig. 4, is well known and will therefore be discussed only briefly. Owing to the odd number of electrons the compound is metallic as seen by the finite number of states at E_F. The Cu d states are found in the same energy range as the oxygen p states between -8 eV and the Fermi level. The center of gravity of the copper states is slightly nearer E_F. The DOS demonstrate that the mixing of the oxygen p with the late transition metal states is strong. We find a different density of oxygen states for the two different oxygen atoms in this structure type. In a manner shared by other cuprate superconductors, the in-plane oxygen O2 interacts more strongly with the copper d states and is therefore twice as broad as the apical oxygen states. Lanthanum states are only found above E_F as the lanthanum atoms are fully ionized. An interesting feature in the DOS is the small van Hove peak 0.06 eV below E_F. This feature has been remarked upon by earlier workers.[40]

3.2 Paramagnetic $La_2CaCu_2O_6$

The densities of state for $La_2CaCu_2O_6$ displayed in Fig. 5 look very similar to the DOS of La_2CuO_4. In this compound too, we observe a significant difference in the partial DOS of the apical O3 and the in-plane oxygen O2 atoms. The apical oxygen partial (p) DOS extends from -4 to -1 eV, with small contributions below and above this range, whereas the band width of the in-plane oxygen is more than 8 eV. The Cu d states extend from -6 eV to E_F, with a few states above E_F. Both oxygen atoms, but mainly the in-plane oxygen states, contribute to small vHS peaks near E_F. From an integration of the density of states we can estimate, assuming rigid-band behaviour, the amount of holes we need to optimally dope the compound to superconductivity, by coinciding the vHS and E_F. The peak is found around 0.24 eV below E_F and in agreement with the experiment, 0.4 holes per formula unit are necessary to achieve coincidence of the vHS and E_F. The second peak is 0.58 eV (and 1.4 holes) below E_F.

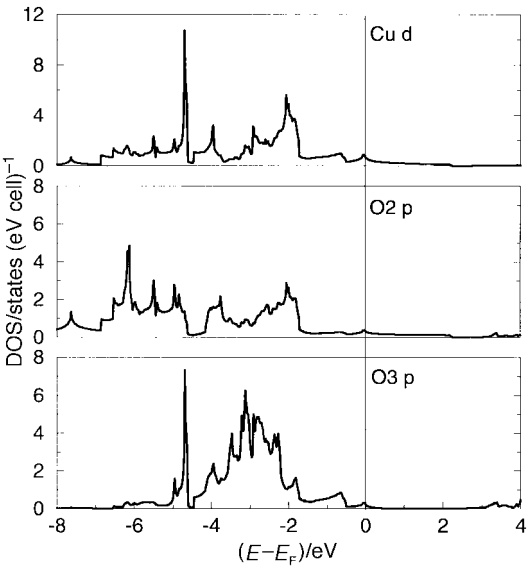

Fig. 4 Partial DOS of paramagnetic La_2CuO_4 from Cu and O orbitals in the vicinity of the Fermi level (which is marked by a vertical line in this and other DOS figures)

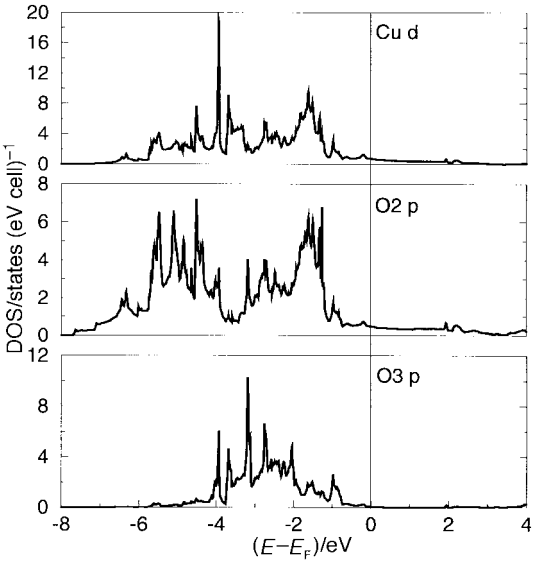

Fig. 5 Partial DOS of paramagnetic $La_2CaCu_2O_6$ from Cu and O orbitals in the vicinity of the Fermi level

3.3 Ferromagnetic $LaSr_2Mn_2O_7$

In Fig. 6 we display the DOS due to the Mn and O atoms of ferromagnetic $LaSr_2Mn_2O_7$. The solid lines are the majority (notionally spin ↑ states) and the dashed lines the minority states (notionally spin ↓). There is only one manganese position in this structure type, so that the number of electrons per manganese is non-integral: $d^{+3.5}$. We therefore expect that $LaSr_2Mn_2O_7$ is a metal. There are a finite number of states at E_F for both spin directions. These states involve the participation of the Mn d and O2 and O3 p orbitals. There is a strong degree of spin polarization for all the atoms displayed in the vicinity of E_F. The presence of minority states at E_F is surprising because we expect a high spin system to have only unoccupied minority d states of Mn. This feature could be a problem of the spherically symmetric potential used within the ASA. However, we recollect that the experimental situation is in keeping with moments less than the spin-only value. For the minority spin density there is a gap between the occupied and the conduction bands, whereas there is no gap in the majority DOS.

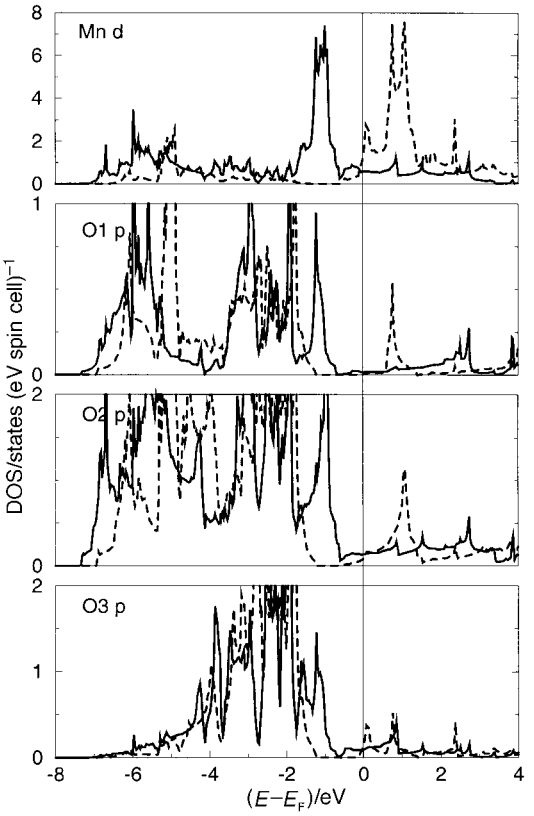

Fig. 6 Partial DOS of ferromagnetic $LaSr_2Mn_2O_7$ from Mn and O orbitals in the vicinity of the Fermi level. The solid curves are the envelope of the majority (spin ↑) states and the dashed curves are the envelope of the minority (spin ↓) states.

The partial DOS of the manganese d states shows fully occupied t_{2g} states between −2 eV and the Fermi energy and some states due to oxygen levels. From the present LSDA calculations we can conclude that the interaction between the transition metal and the oxygen states is less strong in the manganites than in the cuprates. This is as expected from optical gap measurements of the first row transition metal perovskites: that as one traverses the row, the gap has increasing p–d character, implicating greater metal–oxygen covalency for the later 3d metals.[45]

The states at E_F are e_g states which are broader compared with t_{2g} states. The minority states of the Mn d are nearly unoccupied, with t_{2g} states mainly above E_F and a small band width as expected (between 0 and 1.5 eV). As we found in the cuprates the oxygen states of the O2 oxygen atoms within the layers are broad; the majority states extend from −7.5 to −0.5 eV, there are also some states at E_F, but less than when compared with the cuprates. The minority oxygen states are found between −7 and −1.3 eV. The polarization of oxygen states is due to the strong interaction with the polarized Mn d states. The p states of the apical oxygen O1 between the two Mn–O layers are broader (a band width of 7.2 eV for the majority band, and a band width of 5.8 eV for the minority band). The position is the same as for the in-plane O2. However, only O2 and O3 seem to contribute to the states at E_F. The band width of O3 is much smaller owing to the interaction with fewer Mn atoms and because it is further away from Mn than the other oxygen atoms with a width around 4 eV for the majority band and 5 eV for the minority band. Despite using a large number of k points, we cannot see the vHSs within the total DOS.

It is interesting to compare the nature of the bonding due to metal d_{z^2} with oxygen in the $m=2$ cuprate and manganite. The band formed by d_{z^2} and O3 is antibonding. In the cuprate, the Cu–O3 distance is longer than the Mn–O3 distance in the manganite. Additionally, O1 is missing in the cuprate. Both these factors serve to considerably stabilize the d_{z^2} of the cuprate when compared with the manganite.

The result of a metallic DOS is clearly at odds with the negative room-temperature temperature coefficient of resistance (TCR) obtained for all three compounds. The L(S)DA does not explicitly take electron correlation into account, especially, the manner by which electron hopping is hindered by the Coulomb repulsion between electrons and these are clearly important for first row transition metal oxides as pointed out by a number of workers in the field. We note that the band picture can and does correctly predict insulating behaviour in many systems with an even number of electrons in the unit cell. Systems such as La_2CuO_4 are in fact borderline systems in which antiferromagnetic ground states as well as Coulomb correlation (the Hubbard U) can result in band-gaps and vanishing DOS at E_F.[40] If the former effect is active, within an accurate LSDA, a gap can indeed be obtained, provided the spin-polarized calculation is performed on the antiferromagnet. Indeed Satpathy *et al.*[46] do obtain an insulating ground state for $LaMnO_3$ within the LSDA, though they point out that the large on-site Hubbard U which they estimate to be about 9 eV is important in these systems. Our concern here is less with the exact energetics and more with the nature and symmetry of the states near the E_F so we defer discussing the nature of gaps for the present.

Table 1 Total energies for the different magnetic structures of $LaSr_2Mn_2O_7$

structure	energy/eV
ferromagnet	−481 120.00
A-type antiferromagnet	−481 120.27
antiferromagnetic supercell (scaled)	−481 119.73

The high density of states at E_F for this ferromagnetic composition indicates that it would be unstable in keeping with the proposed phase segregation picture put forth for this composition by Battle *et al.*[47] as well as the picture of charge ordering suggested in ref. 30. The fact that the spin-down states are partially occupied reduces the calculated moment of Mn from the spin only value of 3.5 μ_B per Mn to about 3.2 μ_B per Mn. This corresponds to the value obtained for the ferromagnetic composition $La_{1.2}Sr_{1.8}Mn_2O_7$ from magnetization[25] and neutron measurements.[28,29]

3.4 Spin DOS of antiferromagnetic $LaSr_2Mn_2O_7$

The total energies of the ferromagnetic $LaSr_2Mn_2O_7$, the simple A-type antiferromagnet depicted in Fig. 2(a) and the antiferromagnetic supercell depicted in Fig. 2(b) are presented in Table 1. The differences in the energies are marginal, and the most stable spin arrangement seems one of alternating planes of the same spin stacked along the *c* axis of the structure. This is in fact the antiferromagnetic structure observed by Battle *et al.*[47] for one of the two phases in biphasic $LaSr_2Mn_2O_7$ (more precisely, the composition is $La_{0.96}Sr_{2.04}Mn_2O_7$. This is also the magnetic structure of $NdSr_2Mn_2O_7$.[48] The reason for performing a calculation on the supercell shown in Fig. 2(b) is that a charge-ordered ground state as suggested from a combination of transport and magnetic measurements[30] and Mn site alloying experiments[49] is possible with this superstructure. Such charge ordering might be observed if the structure were allowed to relax during the calculation. Fig. 7 compares the spin-up DOS on the two Mn atoms, labelled Mna and Mnb in the simple antiferromagnet with the spin-up DOS on the two different Mn of the antiferromagnetic supercell. Note that the spin-up DOS on Mna exactly coincides with the spin-down DOS on Mnb in both cases.

While there is a clear spin gap of about 1 eV in the antiferromagnetic supercell seen in Fig. 7(b), the DOS of the simple antiferromagnet shown in Fig. 7(a) resembles the ferromagnetic DOS rather strongly. Both the ferromagnet and the simple antiferromagnet share the common feature that within the planes, they are magnetized with the same polarity; the resemblance in the DOS thus suggests that it is the in-plane magnetic coupling that dominates the electronic structure. The position of the E_F is not within the gap states in the case of the antiferromagnetic supercell as seen from Fig. 7(b). The experimental situation is not entirely clear but from Fig. 6(b), we see that if Mna and Mnb were chemically distinct apart from being magnetically distinct, the magnitude of this gap might be larger, yielding a picture of alternating Mn^{III} and Mn^{VI} in the planes coupled with a breathing mode distortion of the surrounding oxygen octahedra. This is the experimental situation in $La_{0.5}Sr_{1.5}MnO_4$.[50] A true gap at E_F might also result if Coulomb correlations of the Hubbard *U* type were explicitly introduced.

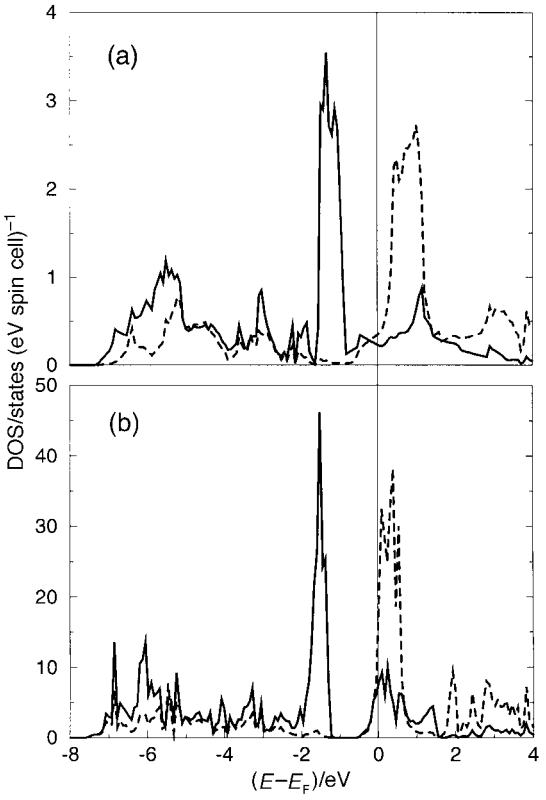

Fig. 7 (a) Spin ↑ DOS on the Mna (solid) and Mnb (dashed) for the simple antiferromagnet represented in Fig. 2(a). (b) Spin ↑ DOS on the Mna (solid) and Mnb (dashed) for the antiferromagnetic supercell represented in Fig. 2(b). Note that the DOS due to spin ↑ Mna corresponds to the DOS due to ↓ Mnb.

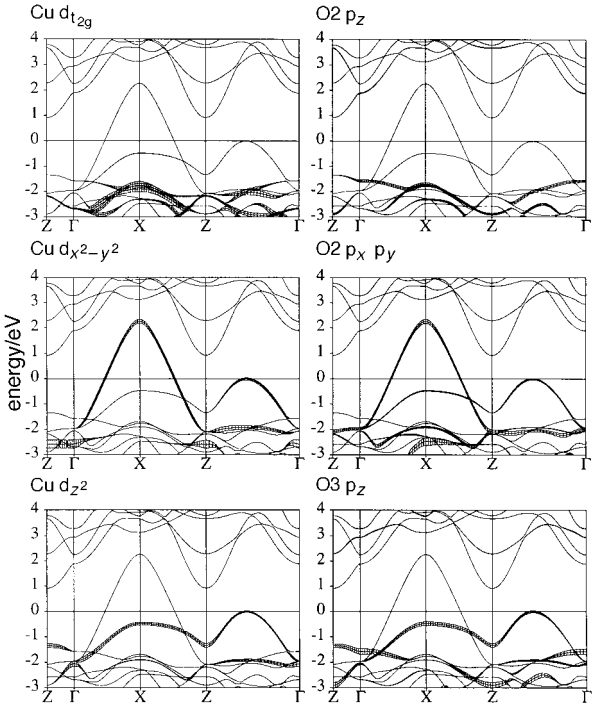

Fig. 8 Important Cu and O fatbands of La_2CuO_4 in a small energy window around E_F. In this and the other fatband structures, 100% orbital character is indicated by a width of 0.175 eV.

4 Band structures

4.1 La_2CuO_4

Fig. 8 shows the fatbands derived from different atomic orbitals of La_2CuO_4. The Cu t_{2g} bands are fully occupied in this compound and are low in energy. Only the upper portion of this fatband is shown in Fig. 8. Cu d_{xz} d_{yz} have a π bonding interaction with the in-plane O2 p_z as seen from the fatbands derived from these orbitals, particularly at the X point. Only one band crosses E_F. It is a highly disperse band. A second flat band is slightly below E_F and touches the Fermi level between Γ and Z. From Fig. 8, we see that the highly disperse

band comprises states derived from the Cu $d_{x^2-y^2}$ strongly overlapped with in-plane oxygen O2 p_x p_y states. This band is antibonding. It shows no dispersion along Z–Γ which is perpendicular to the planes. The cause for the high dispersion within the layers (Γ–X–Z) is that the lobes of the $d_{x^2-y^2}$ orbital points directly towards the four O2 oxygen neighbors within the layers. A hopping of electrons to neighboring Cu atoms is thus possible through the chess-board like ordering of the Cu atoms. For such strong metal–oxygen overlap, it is also necessary that the metal d levels are of nearly the same energy as the oxygen p levels and this seems to be the case in this structure type, particularly for the late transition metals. The main contribution to the flat band slightly below E_F comes from the Cu d_{z^2} and the apical oxygen p_z orbital from O3 which are directed onto one another. The Cu s states also contribute to this band, but are above E_F. As expected, this d_{z^2} band has some dispersion perpendicular to the plane along Z–Γ in which region it is split up into two bands. This dispersion is much less compared than the width of the Cu–O band in the plane, owing to the longer out-of-plane Cu–O bond lengths. The most important feature of this band structure is the hybridization of the two e_g bands between Γ and Z (Z in the next BZ), which leads to the saddle point. A similar situation is also found in other cuprate superconductors. We note from this figure (Fig. 8) and in the next one, of the fatbands of $La_2CaCu_2O_6$ (Fig. 9), that the O2 p_z orbital is not of interest in that it does not participate in the states near the Fermi level. It is however involved in forming the pdπ* band with the Cu d_{xz} d_{yz} orbitals.

4.2 $La_2CaCu_2O_6$

A similar bonding interaction is found for $La_2CaCu_2O_6$, whose important fatbands in the vicinity of E_F are presented in Fig. 9. The main difference is the observation of two nearly degenerate bands along Γ–X–Z because of the bi-layered nature of the structure. Another difference is that one missing oxygen in the Cu–O polyhedra (square pyramid instead of octahedra) stabilizes considerably a branched Cu d_{z^2} derived band. Two saddle points, one 0.24 eV and the second, which is bifurcated, 0.58 eV below E_F can be found in the Γ and Z (Z in the next BZ) region of the band structure. They arise, as in La_2CuO_4, largely due to the fact that Cu d_{z^2} does not bond very strongly in the plane. The overall band width of the pdσ* band is the same as in La_2CuO_4 indicating a similar bonding strength within the layers. The overall band width of the d_{z^2} band is smaller than what is observed in La_2CuO_4 because the Cu are bound to O only on one side. In keeping with the formal d^9 electron count in this compound and the square pyramidal coordination of Cu, the d_{z^2} band is totally occupied and the highly disperse band derived from strongly mixed $d_{x^2-y^2}$ and in-plane O2 p_x p_y orbitals (the pdσ* band) is half filled.

4.3 Ferromagnetic $LaSr_2Mn_2O_7$

We now discuss in some detail the band structure of this compound. Fig. 10 shows the important majority (spin ↑) fatbands of ferromagnetic $LaSr_2Mn_2O_7$ within a 7 eV window around the Fermi level. The crystal field splitting separates the t_{2g} levels from the d_{z^2} and the $d_{x^2-y^2}$ orbitals by about 1 eV (taking the smallest value). The elongation of the apical bonds in the MnO_6 octahedra should split e_g. Mn^{III} is a well known Jahn–Teller system, but the splitting of the t_{2g} and e_g states cannot be ascribed to this cause within the present calculation framework. Apart from the crystal field and the elongation of the octahedra, there is also an exchange splitting of about 2 eV due to spin polarization as we saw in the DOS. Minority t_{2g} (not shown) make a large contribution to the DOS at E_F as we have remarked earlier. This could be an artifact of the LSDA. In the principle Γ–X and X–Z directions which correspond to bonding in the plane, the dispersion of the t_{2g} bands are not very large. The t_{2g} level is also less stabilized in comparison with the cuprates because of smaller filling. In the Z–Γ direction which is indicative of bonding along the z direction, the dispersion is small in agreement with the general understanding that these phases are strongly two-dimensional, but is larger than in the cuprates. As in the cuprates, the overlap of Mn $d_{x^2-y^2}$ with in-plane O2 p_x p_y gives rise to a highly disperse band in the Γ–X–Z region of the band structure. Note from fatband widths, however, that the metal derived states contribute a greater weight to this band than the oxygen

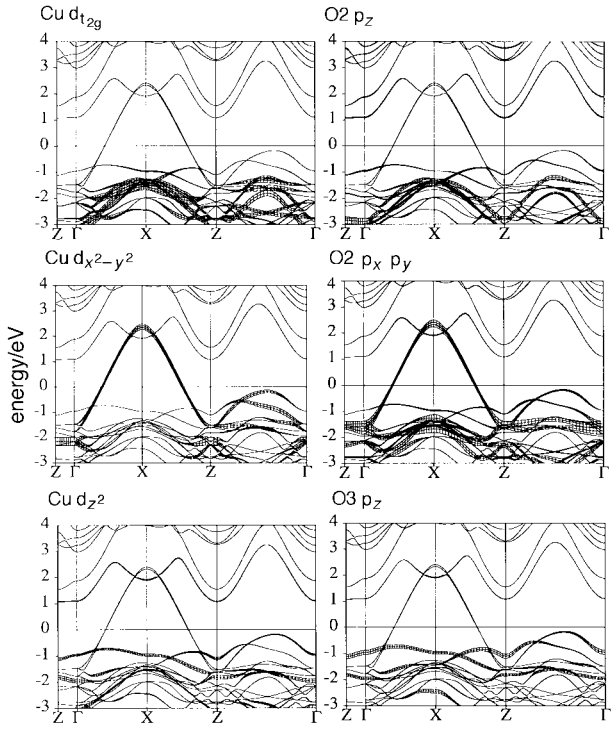

Fig. 9 Important Cu and O fatbands of $La_2CaCu_2O_6$

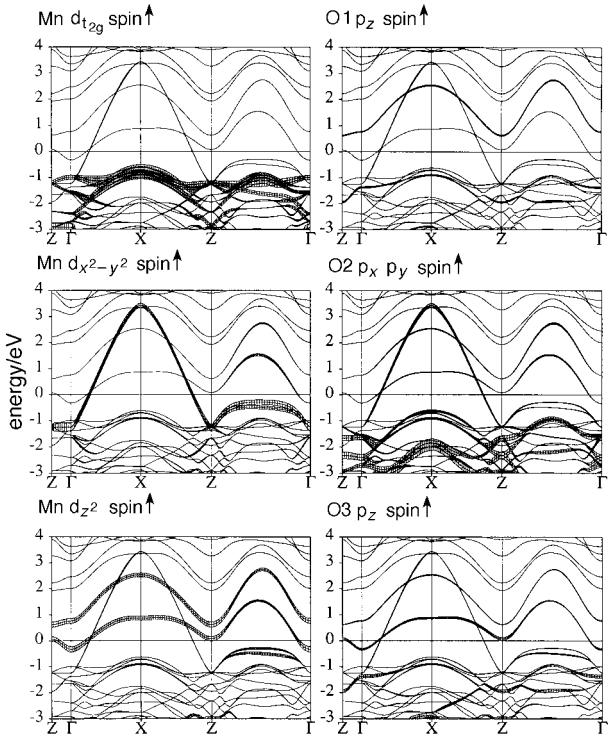

Fig. 10 Important spin ↑ fatbands of ferromagnetic $LaSr_2Mn_2O_7$

derived states in contrast to the cuprates where the contribution is about equal. This trend has been noted in the discussion of the DOS. The width of the majority band is about 4 eV. The width is large enough that the tetragonal splitting of the e_g level (to stabilize Mn d_{z^2} over Mn $d_{x^2-y^2}$) is obscured in Fig. 10. The Mn d_{z^2} majority bands are split because there are Mn–O–Mn interactions only on one side. In other words, the two apical oxygen atoms in each MnO_6, namely O1 and O3, are not equivalent. The consequences of this d_{z^2} splitting are significant and discussed presently. What is interesting is the very flat branch of the majority d_{z^2} hybridised with $d_{x^2-y^2}$ bands in the Γ–Z direction (Z in next BZ). The flatness or lack of dispersion is merely a manifestation of the weak bonding involvement of the out-of-plane orbitals.

We now discuss the oxygen participation near the E_F shown as fatbands in Fig. 10. As anticipated, the O2 p_x and p_y orbitals are strongly mixed in the majority band derived from the Mn $d_{x^2-y^2}$ orbitals. The in-plane p_z orbitals (not shown) are seen not to bind very strongly to Mn d_{z^2} near the Fermi energy. The p_z orbitals on the apical oxygen atoms O1 and O3 show some interesting features as observed from the fatbands shown in Fig. 10. The p_z orbitals on O1 and O3 from σ bonding and antibonding bands with the d_{z^2} orbitals on Mn. The presence of two Mn in the unit cell further splits these bands through interaction with one another giving two bonding and two antibonding bands each for the Mn–O1 and Mn–O2 interactions. The antibonding bands are near the Fermi energy and are clearly seen in the fatband representation along the Z–Γ direction (Z along c^*). The Mn–O1 distance ($d_{Mn-O1} = 1.95$ Å) is shorter than the Mn–O3 distance ($d_{Mn-O3} = 1.98$ Å). As a result, the two branches of the Mn d_{z^2} O1 p_z σ* orbital derived bands are simultaneously more stabilized and destabilized than the branches of the Mn d_{z^2} O3 p_z σ* derived bands, and while the latter fortuitously crosses E_F, the upper branch of the former is about 0.8 eV above E_F in the Z–Γ region of the BZ. The splitting of the majority Mn d_{z^2} fatbands near E_F is thus linked with the lower branch being overlapped with O3 p_z and the upper branch with O1 p_z. The consequences are as follows. (1) On replacing La by smaller lanthanoids (Pr, Nd, *etc.*) in $(LnSr)_3Mn_2O_7$ the transition from a paramagnetic insulator to a ferromagnetic metal (as observed in the La compound) is not observed. This can now be ascribed to the elongation of d_{Mn-O3} (observed in experiment) stabilizing the lower d_{z^2} branch thus moving the instability in the DOS to E_F. This results in antiferromagnetic insulating ground states. (2) On replacing La by smaller lanthanoids and on cooling, the nature of the Jahn–Teller like distortion is '5-in, 1-out' rather than the usual D_{4h} '4-in, 2-out'. There are also unusual pressure dependences of the Mn–O bond lengths. These are clearly related to the branched structure of the Mn d_{z^2} fatband.

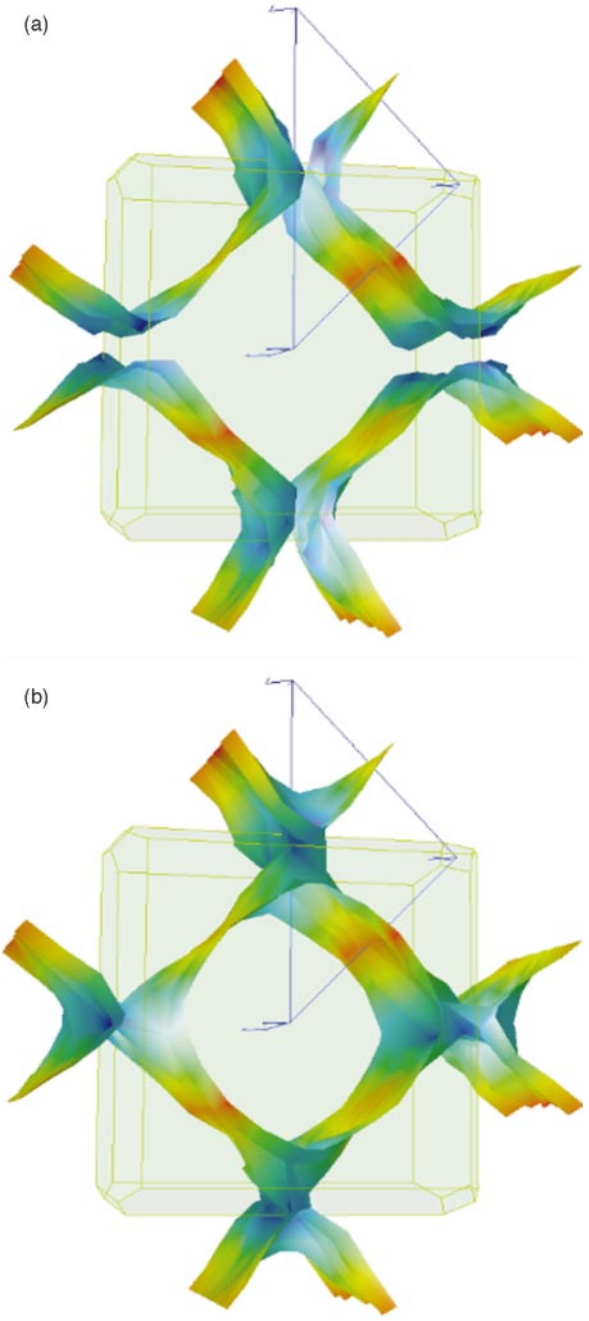

Fig. 11 (a) LMTO-ASA Fermi surface of paramagnetic La_2CuO_4. (b) Energy isosurface of La_2CuO_4 at a constant energy 0.06 eV below E_F. In both figures, the colours represent the velocities and thus the dispersion. A shading from red to blue indicates regions of high and low velocities respectively in this and the next two figures.

4.4 Fermi surfaces

The Fermi surfaces of La_2CuO_4, $La_2CaCu_2O_6$ and $LaSr_2Mn_2O_7$ are shown in Fig. 11, 12 and 13. The representation is looking down c^* perpendicular to the plane which contains Γ–X and the Z in the neighboring BZ. One Z point falls nearly on the top of the Γ point. Because of the body centering the Z points of the neighbouring Brillouin zone are in the same plane as the Γ point. The colours of the plots reflect the Fermi velocity, where red means a high Fermi velocity and blue a low Fermi velocity.

Our three-dimensional visualisation of the Fermi surface is in good agreement with the known LDA Fermi surface of tetragonal undistorted La_2CuO_4. In case of tetragonal La_2CuO_4, a relative simple and roughly two-dimensional Fermi surface is seen in Fig. 11(a). The thickness of the Fermi surface in the plane of the representation and the structure of the Fermi surface along Γ–Z suggests that there is a small three-dimensional contribution. From the band structure calculation we know that only one, the half-filled pdσ* band, crosses E_F. Therefore there is only one envelope of the Fermi surface. For a simple half-filled square net we expect square cylinders with electrons around Γ and holes around X and perfect nesting with $q = (\pi/a, \pi/a, 0)$. The Fermi surface of La_2CuO_4 seen here consists of X centered cylinders of holes with four sharp knobs and a nesting vector slightly larger than $q = (\pi/a, \pi/a, 0)$. We know from the density of states and the band structure, that there is a DOS peak (a vHS) associated with a saddle point in the energy isosurface ε_k about 0.06 eV below E_F. We therefore chose this energy to construct an energy isosurface shown in Fig. 11(b). Note that in a sense, we are doping holes by considering such energy isosurfaces. The isosurface takes on an X-shape around 0.4 along the Γ–Z (Z in next BZ) direction. A further reduction of the energy of the isosurface leads to cylinder now centered around Γ but with

a nesting vector of the same order [slightly smaller than $q=(\pi/a, \pi/a, 0)$]. Around the saddle point along the Γ–Z direction (Z in next BZ), the blue color of the FS demonstrate local states (small Fermi velocity) whereas the Fermi velocity is high, when the isosurface cuts the Γ–X direction.

Since $La_2CaCu_2O_6$ has two Cu–O layers per unit cell which should be rather weakly coupled, a pair of layer-derived CuO_2 pdσ* bands are expected to cross the Fermi level, each similar to the corresponding band in La_2CuO_4. Therefore the calculated Fermi surface [Fig. 12(a)] consists of two nearly degenerate envelopes (cylinders around the X point) arising from the two Cu–O layers. It should be noted that these surfaces must be regarded not as arising individually from the two layers but rather as due to bonding and antibonding combinations of the states of the Cu–O layers. Compared with the Fermi surfaces of La_2CuO_4 this Fermi surface is less three-dimensional as can seen by the fact that the in-plane thickness of each envelope is very small and there is no structure along Γ–Z. The knobs of this FS are also less sharp. In this compound there are large flat portions in blue regions perpendicular to the (Γ–Z) direction. Because of the two saddle points along the Γ–Z direction we plot two energy isosurfaces for $\varepsilon_k = E_F - 0.24$ eV and for $\varepsilon_k = E_F - 0.58$ eV as seen in Fig. 12(b) and (c). If the Fermi energy coincides with the first saddle point, the isosurface shows one cylindrical envelope around X, which belongs to the second band and one X-shape nesting nearly halfway between Γ and Z (Z in next BZ). This leads to a surface of two cylinders, one with electrons around Γ and one with holes around X. If the isosurface touches the second saddle point, we observe an X-shape nesting for the second band with cylinders that have sharp knobs. The electrons are around Γ and holes around X and the cylindrical energy isosurface of round knobs has electrons around Γ of the first band. The energy isosurface for an energy slightly above both saddle points are two cylinders with different radii around Γ.

In Fig. 13 we see the Fermi surface of the CMR system $LaSr_2Mn_2O_7$. In addition to the two cylinders, which show similar energy behavior to the energy isosurfaces of $La_2CaCu_2O_6$, we observe a three-dimensional Fermi surface along Γ–Z where Z refers to $(0, 0, \pi/2c)$. This feature exists in the undoped compound and reflects on one hand the greater three-dimensionality of the overall band structure and on the other hand that the d_{z^2} is not fully occupied. The Fermi surface has no structure along Γ–Z and sharper knobs when compared with $La_2CaCu_2O_6$. The blue regions (of low Fermi velocity) are larger and only at a part of the Fermi surface along Γ–X is the velocity high. Also in this system, there are holes around X and electrons around Γ.

5 Conclusions

An analysis of the TB-LMTO band structure in the vicinity of the Fermi energy in conjunction with the powerful 'fatband' representation allows a clear view of the states that contribute to conductivity and magnetism in the three compounds studied. Comparing the manganite with the cuprate, the differences in the electronic structure arise because of the different filling of the frontier d levels and the spin-polarization in the case of the manganite. More subtle differences can be accounted for by the distinct MO polyhedra of the three compounds studied. The nature of bands in the principle bonding direction Γ–X seem to be similar in the cuprates and the manganites. Strong bonding in the plane between metal $d_{z^2-y^2}$ and O p_x p_y lead to disperse $d_{x^2-y^2}$ bands whose bandwidth hides the Jahn–Teller distortion. The metal d_{z^2} level is flat because it is not very strongly bound in the Γ–X direction. This flat band results in the van Hove-like features in all three compounds studied. These features have been easily visualised through the use of energy isosurfaces and Fermi surfaces.

The interesting feature in these band structures seems to be

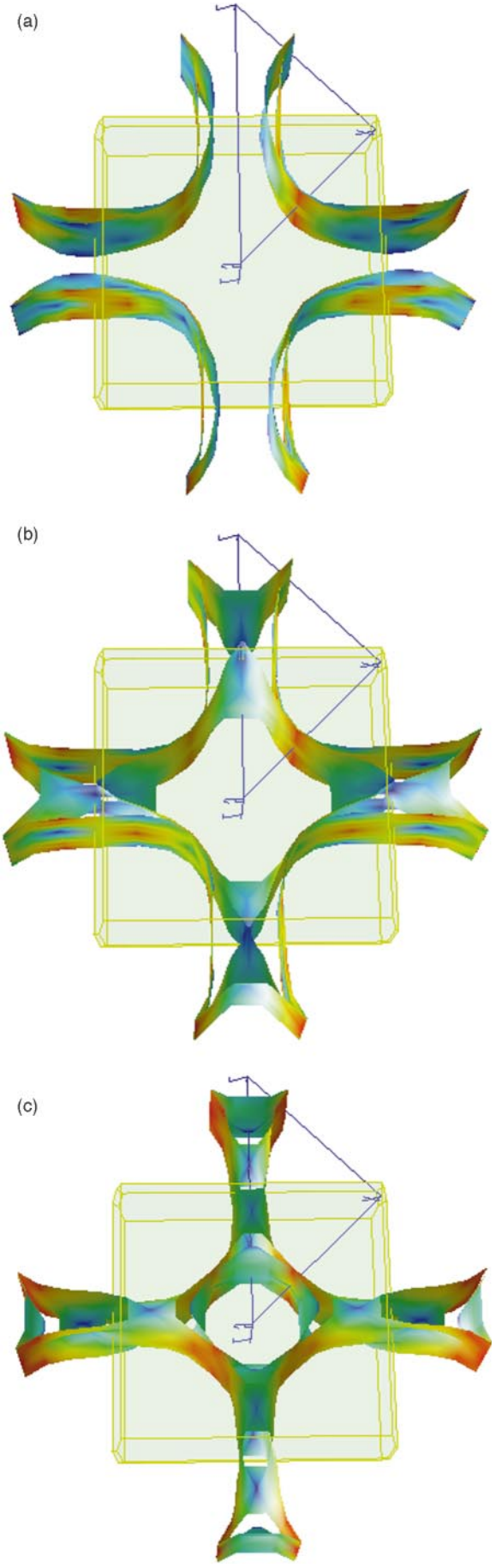

Fig. 12 (a) LMTO-ASA Fermi surface of paramagnetic $La_2CaCu_2O_6$. (b) Energy isosurface of $La_2CaCu_2O_6$ at a constant energy 0.24 eV below E_F. (c) Energy isosurface of $La_2CaCu_2O_6$ at a constant energy 0.58 eV below E_F.

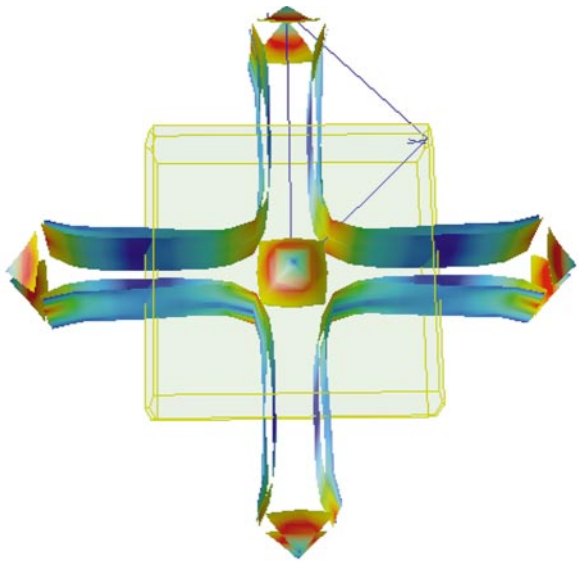

Fig. 13 LMTO-ASA Fermi surface of ferromagnetic $LaSr_2Mn_2O_7$

the combination of flat and disperse bands in the vicinity of the Fermi surface. The former lead to unstable Fermi surfaces (leading to interesting low-temperature properties) and the dispersion of the latter allow conducting ground states. These observations tempt us to speculate that in a given structure type, it is the filling of the electrons in the frontier orbitals and their spin state that governs the nature of the ground state. While this might seem self-evident, the consequences are that when the existence of a particular ground state in a given structure type is established, one can look for other phenomena by playing with the electronic filling and the spin states.

References

1 R. von Helmholt, J. Wecker, B. Holzapfel, L. Schultz and K. Samwer, *Phys. Rev. Lett*., 1993, **71**, 2331.
2 R. M. Kusters, J. Singleton, D. A. Keen, R. McGreevy and R. Hayes, *Physica B*, 1989, **155**, 362.
3 K. Chahara, T. Ohno, M. Kasai and Y. Kozono, *Appl. Phys. Lett*., 1993, **63**, 1990.
4 S. Jin, T. H. Tiefel, M. McCormack, R. A. Fastnacht, R. Ramesh and L. H. Chen, *Science*, 1994, **264**, 413.
5 G. Briceno, H. Chang, X. Sun, P. G. Shultz and X. D. Xiang, *Science*, 1995, **270**, 273.
6 R. Mahendiran, A. K. Raychaudhuri, A. Chainani and D. D. Sarma, *J. Phys. Condens. Matter*, 1995, **7**, L561.
7 A. P. Ramirez, R. J. Cava and J. Krajewski, *Nature* (*London*), 1997, **386**, 156.
8 A. Maignan, R. Seshadri, C. Martin, F. Letouzé and B. Raveau, *Solid State Commun*., 1997, **102**, 551.
9 W. Archibald, J.-S. Zhou and J. B. Goodenough, *Phys. Rev. B*, 1996, **53**, 14445.
10 H. W. Hwang, S.-W. Cheong, P. G. Radaelli, M. Marezio and B. Batlogg, *Phys. Rev. Lett*., 1995, **75**, 914.
11 D. M. Newns, H. R. Krishnamurthy, P. C. Pattnaik, C. C. Tsuei, C. C. Chi and C. L. Kane, *Physica B*, 1993, **186**, 801.
12 D. L. Novikov and A. J. Freeman, *Physica C*, 1993, **216**, 273.
13 A. Asamitsu, Y. Moritomo, Y. Tomioka, T. Arima and Y. Tokura, *Nature* (*London*), 1995, **373**, 407.
14 J. M. DeTeresa, M. R. Ibarra, P. A. Algabarel, C. Ritter, C. Marquina, J. Blasco, J. García, A. del Moral and Z. Arnold, *Nature* (*London*), 1997, **386**, 256.
15 S. N. Ruddlesden and P. Popper, *Acta. Crystallogr*., 1958, **11**, 54.
16 H. Shaked, P. M. Keene, J. C. Rodriguez, F. F. Owen, R. L. Hitterman and J. D. Jorgensen, *Crystal Structures of the High-T_c Superconducting Copper-Oxides*, Elsevier, Amsterdam, 1994.
17 G. H. Jonker and J. H. van Santen, *Physica*, 1950, **16**, 377.
18 J. F. MacChesney, J. F. Potter and R. C. Sherwood, *J. Appl. Phys*., 1969, **40**, 1243.
19 R. A. Mohan Ram, P. Ganguly and C. N. R. Rao, *J. Solid State Chem*., 1987, **70**, 82.
20 C. Zener, *Phys. Rev*., 1951, **82**, 403.
21 Y. Moritomo, A. Asamitsu, H. Kuwahara and Y. Tokura, *Nature* (*London*), 1996, **380**, 141.
22 R. Mahesh, R. Mahendiran, A. K. Raychaudhuri and C. N. R. Rao, *J. Solid State Chem*., 1996, **122**, 448.
23 R. Seshadri, C. Martin, M. Hervieu, B. Raveau and C. N. R. Rao, *Chem. Mater*., 1997, **9**, 270.
24 P. D. Battle, M. A. Green, N. S. Laskey, J. E. Millburn, M. J. Rosseinsky, S. P. Sullivan and J. F. Vente, *Chem. Commun*., 1996, 767.
25 R. Seshadri, C. Martin, A. Maignan, M. Hervieu, B. Raveau and C. N. R. Rao, *J. Mater. Chem*., 1996, **6**, 1585.
26 P. Laffez, G. van Tendeloo, R. Seshadri, M. Hervieu, C. Martin, A. Maignan and B. Raveau, *J. Appl. Phys*., 1996, **80**, 5850.
27 P. D. Battle, S. J. Blundell, M. A. Green, W. Hayes, H. Honold, A. K. Klehe, N. S. Laskey, J. E. Millburn, L. Murphy, M. J. Rosseinsky, N. A. Samarin, J. Singleton, N. E. Sluchanko, S. P. Sullivan and J. F. Vente, *J. Phys. Condens. Matter*, 1996, **8**, L427.
28 J. F. Mitchell, D. N. Argyriou, J. D. Jorgensen, D. G. Hinks, C. D. Potter and S. D. Bader, *Phys. Rev. B*, 1997, **55**, 63.
29 D. N. Argyriou, J. F. Mitchell, J. B. Goodenough, O. Chmaissem, S. Short and J. D. Jorgensen, *Phys. Rev. Lett*., 1997, **78**, 1568.
30 R. Seshadri, A. Maignan, M. Hervieu, N. Nguyen and B. Raveau, *Solid State Commun*., 1997, **101**, 453.
31 P. D. Battle, M. A. Green, N. S. Laskey, J. E. Millburn, L. Murphy, M. J. Rosseinsky, S. P. Sullivan and J. F. Vente, *Chem. Mater*., 1997, **9**, 552.
32 R. Seshadri, M. Hervieu, C. Martin, A. Maignan, B. Domenges, B. Raveau and A. Fitch, *Chem. Mater*., 1997, **9**, 177.
33 L. M. Rodriguez-Martinez and J. P. Attfield, *Phys. Rev. B*, 1996, **54**, 15622.
34 W. E. Pickett and D. J. Singh, *Europhys. Lett*., 1995, **32**, 759.
35 R. J. Cava, B. Batlogg, R. B. van Dover, J. J. Krajewski, J. V. Waszczak, R. M. Fleming, W. F. Peck Jr., L. W. Rupp, P. Marsh, A. C. W. P. James and L. F. Schneemeyer, *Nature* (*London*), 1990, **345**, 602.
36 A. Fuertes, X. Obradors and J. M. Navarro, *Physica C*, 1990, **170**, 153.
37 R. J. Cava, A. Santoro, J. J. Krajewski, R. M. Fleming, J. V. Waszczak, W. F. Peck Jr. and P. Marsh, *Physica C*, 1990, **172**, 138.
38 O. Jepsen and O. K. Andersen, *Z. Phys. B*, 1995, **97**, 35.
39 D. Johrendt, C. Felser, O. Jepsen, O. K. Andersen, A. Mewis and J. Rouxel, *J. Solid State Chem*., 1997, **129**, 254.
40 W. E. Pickett, *Rev. Mod. Phys*., 1989, **61**, 433.
41 C. J. Bradley and A. P. Cracknell, *The mathematical theory of symmetry in solids*, Clarendon Press, Oxford, 1972.
42 G. Krier, O. Jepsen, A. Burckhardt and O. K. Anderson, TB-LMTO-ASA47, MPI für Festkörperforschung, Stuttgart, Germany, 1996.
43 H. L. Skriver, *The LMTO method*, Springer, Berlin, 1984.
44 G. Krier, O. Jepsen and O. K. Andersen, unpublished results.
45 T. Arima, Y. Tokura and J. B. Torrance, *Phys. Rev. B*, 1993, **48**, 17006.
46 S. Satpathy, Z. S. Popović and F. R. Vukajlović, *Phys. Rev. Lett*., 1996, **76**, 960.
47 P. D. Battle, D. E. Cox, M. A. Green, J. E. Millburn, P. G. Radaelli, M. J. Rosseinsky, L. E. Spring and J. F. Vente, *Chem. Mater*., 1997, **9**, 1042.
48 P. D. Battle, M. A. Green, N. S. Laskey, J. E. Millburn, P. G. Radaelli, M. J. Rosseinsky, S. P. Sullivan and J. F. Vente, *Phys. Rev. B*, 1996, **54**, 15967.
49 C. Martin, A. Maignan and B. Raveau, personal communication.
50 Y. Moritomo, Y. Tomioka, A. Asamitsu and Y. Tokura, *Phys. Rev. B*, 1995, **51**, 3297.

Paper 7/06965K; 26*th September*, 1997